Open access • Journal Article • DOI:10.1364/AO.57.000D74

Eddy current pulsed thermography for ballistic impact evaluation in basalt-carbon hybrid composite panels. — Source link

Hai Zhang, Stefano Sfarra, Ahmad Osman, Fabrizio Sarasini ...+4 more authors

Institutions: Laval University, University of L'Aquila, Fraunhofer Society, Sapienza University of Rome

Published on: 20 Jun 2018 - Applied Optics (Optical Society of America)

Topics: Thermography and Ballistic impact

Eddy Current Pulsed Thermography for Ballistic Impact Evaluation in Basalt-Carbon Hybrid Composite Panels

HAI ZHANG[1,+,*], STEFANO SFARRA[2,3], AHMAD OSMAN[4,5], FABRIZIO SARASINI[6], UDO NETZELMANN[4], STEFANO PERILLI[2], CLEMENTE IBARRA-CASTANEDO[1], AND XAVIER P.V. MALDAGUE[1]

[1] Computer Vision and Systems Laboratory (CVSL), Department of Electrical and Computer Engineering, Laval University, Quebec, G1V 0A6, Canada
[2] Department of Industrial and Information Engineering and Economics, University of L'Aquila, 67100 L'Aquila, Italy
[3] Tomsk Polytechnic University, Thermal Control Methods Laboratory, Tomsk, 634050, Russia
[4] Department of Inspection of Components and Assemblies, Fraunhofer-Institute for Nondestructive Testing IZFP, 66123 Saarbruecken, Germany
[5] University of Applied Sciences Saarland, htw saar, 66117 Saarbruecken, Germany
[6] Department of Chemical Engineering Materials Environment, Sapienza University of Rome, 00184 Rome, Italy
[+] Current address: Center for Advanced Diffusion-Wave Technologies (CADIFT), Department of Mechanical and Industrial Engineering, University of Toronto, 5 King's College Road, Toronto, ON M5S 3G8, Canada
[*] Corresponding author: hai.zhang.1@ulaval.ca

Compiled March 4, 2018

In this paper, eddy current pulsed thermography was used to evaluate ballistic impact damages in basalt-carbon hybrid fiber-reinforced polymer composite laminates for the first time. In particular, different hybrid structures including intercalated stacking and sandwich-like sequences were used. Pulsed phase thermography, wavelet transform, principle component thermography and partial least square thermography were used to process the thermographic data. Ultrasound C-scan testing and X-ray computed tomography were also performed for comparative purposes. Finite element analysis was used for validation. Finally, an analytical and comparative study was conducted based on signal-to-noise ratio analysis.

OCIS codes: (140.3490) Infrared; (060.2420) Thermal imaging;(060.3735) Nondestructive testing.

http://dx.doi.org/10.1364/ao.XX.XXXXXX

NOMENCLATURE

BCB	Basalt-carbon-carbon stacking sequence
CBC	Carbon-basalt-carbon stacking sequence
CT	X-ray computed tomography
ECPT	Eddy current pulsed thermography
EOF	Empirical orthogonal function
FEA	Finite element analysis
INT	Intercalated structure
PCT	Principle component thermography
PLST	Partial least square thermography
PPT	Pulsed phase thermography
SAN	Sandwich-like structure
SNR	Signal-to-noise ratio
UT	Ultrasound C-scan testing
WT	Wavelet transform

1. INTRODUCTION

The evaluation of impact damages at the ballistic level in composite laminates, which have been considered as structural material in military vehicles, is becoming increasingly important. Military vehicles are usually designed to withstand a given ballistic impact. In the design, the weight must be reduced to the maximum extent, but the structure must retain the load-carrying abilities after a ballistic impact. With these needs, fiber-reinforced plastic (FRP) has been considered as a potential alternative to metals for military vehicle design. Nowadays, FRP based on aramid and ultra-high-molecular-weight polyethylene (UHMWPE) fibers have been used in body armors. However, aramid fiber has a low longitudinal compressive strength, polyethylene fiber has a relatively low temperature tolerance, and both of them have a poor matrix compatibility. These drawbacks restrict their use in military vehicles [1].

It has been proven that fiber hybridization is an effective

approach to enhance the impact resistance of FRP, and its improvement is dependent on the positioning and dispersion of the different fibrous layers [2–4]. Recently, fiber hybridization is attracting increasing attention to gain a more gradual failure in brittle composites, a behavior similar to the one exhibited by metals and therefore referred to as pseudo-ductility [5–7]. An established strategy is the hybridization of carbon-glass fibers. This strategy combines the advantages of high strength and high stiffness from carbon fiber and the advantage of high toughness from glass fiber [8–10]. However, glass fiber has the disadvantage of a long degradable durability as a synthetic material [11]. In this regard, basalt fiber, as a natural material, has been considered as an alternative to glass fiber taking into account the environmental benefits [12]. In this framework, an effective non-destructive testing & evaluation (NDT&E) technique for basalt-carbon fibers hybrid materials is needed.

Infrared thermography (IRT) [13], as a widely used NDT&E technique, has been used for the evaluation of composite materials [14–16]. *E.g.*, optical excitation thermography (OET) [17] and vibrothermography (VT), based on the established heating methods, have been used for basalt-carbon fibers hybrid composite laminate evaluation [18]. Compared to ultrasound and x-ray, infrared has the advantages of fast and safe inspection, inexpensive cost, contactless, high spatial resolution and fast acquisition rate [19]. Other emerging NDT&E techniques such as terahertz imaging cannot work on carbon fiber because its electric conductivity disturbs the polarization [20–23]. Therefore, the study on emerging infrared excitation methods such as laser is attracting more attention for hybrid composite evaluation [24]. In this regard, eddy current pulsed thermography (ECPT) is also gaining increasing attention as an emerging approach.

In this paper, ECPT was used to evaluate ballistic impact damages in four basalt-carbon hybrid fiber-reinforced polymer composite laminates for the first time. They have sandwich-like (SAN) and intercalated (INT) structures with carbon-basalt-carbon (CBC) or basalt-carbon-basalt (BCB) stacking sequences, respectively. Pulsed phase thermography (PPT), wavelet transform (WT), principle component thermography (PCT) and partial least square thermography (PLST) were used to process the thermographic data. Ultrasound C-scan testing (UT) and X-ray computed tomography (CT) were also performed for comparative purposes. Finite element analysis (FEA) was used for validation. Finally, an analytical and comparative study was conducted based on signal-to-noise ratio (SNR) analysis.

2. SPECIMENS

The composite panels were produced by autoclave forming using plain weave basalt ($220 g/m^2$) and carbon fibre ($160 g/m^2$) reinforced epoxy prepregs with the same epoxy matrix (DT150). The composites were manufactured through a prepreg lay-up process with a ($0°/90°$) sequence and subsequent autoclave processing. The laminates were cured in SAN and INT structures as shown in Table 1 and in Fig. 1. An impact testing was performed for each configuration using a helium gasgun with a spherical tempered steel projectile (mass = 1.725 g, diameter = 7.5 mm). The impact speeds were 253.46 m/s for SAN and 230.74 m/s for INT. The impact speed was obtained from a high speed camera. The laminate dimension is 100 mm × 100 mm as shown in Fig. 2.

The samples were mounted in a simply supported boundary condition along their edges using aluminum guides. To measure impact and residual velocity, the tests were monitored using

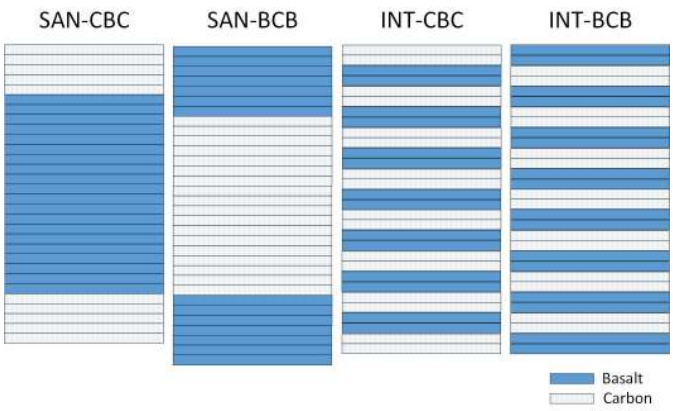

Fig. 1. Schematic structures of the specimens.

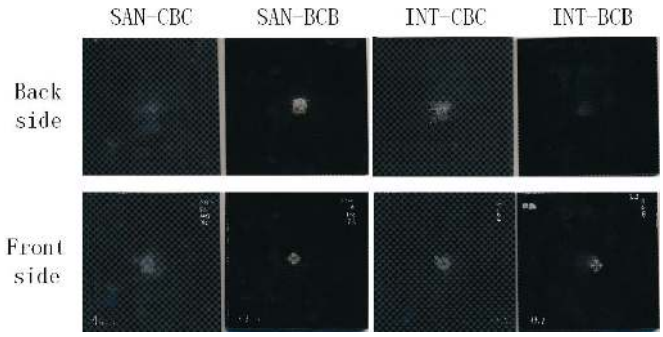

Fig. 2. Photographs of the specimens.

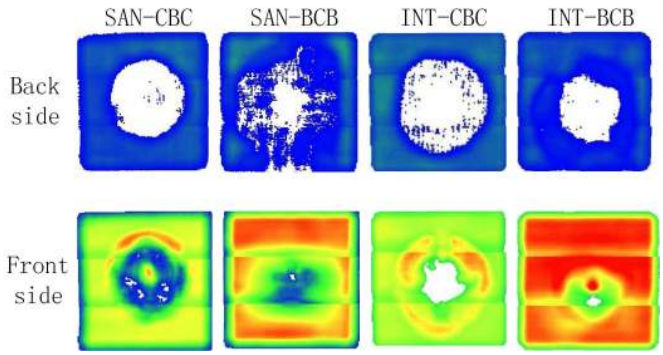

Fig. 3. UT results at 2.25 MHz.

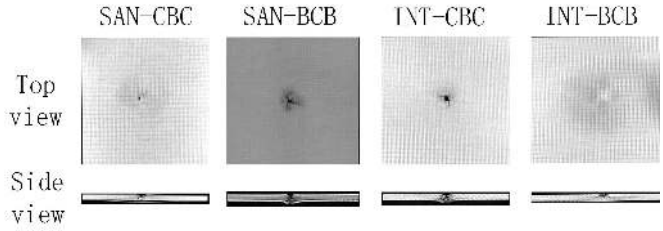

Fig. 4. CT slices at 100μm resolution.

Table 1. Summary of the specimens

Structure	Stacking sequence	Fiber volume fraction	Density $[g/cm^3]$	Thickness $[mm]$	Impact velocity $[m/s]$
SAN-CBC	$[C_5/B_{10}]_s$	0.63 ± 0.01	1.87 ± 0.02	4.00 ± 0.05	251.71
SAN-BCB	$[B_7/C_9]_s$	0.61 ± 0.01	1.72 ± 0.02	4.40 ± 0.06	201.69
INT-CBC	$[(C_2/B_2)_3/C_2/B]_s$	0.60 ± 0.01	1.71 ± 0.01	4.30 ± 0.05	253.46
INT-BCB	$[(B_2/C_2)_3/B_2/C]_s$	0.61 ± 0.01	1.77 ± 0.02	4.20 ± 0.05	248.22

a high speed digital camera APX FASTCAM by Photron with a data-acquisition system set to take 36000 frames/s placed beside the sample holder. For better recording quality, a high intensity halogen light M18 by ARRI was used. The image acquisition is fundamental since the gathered data are processed by Photron FASTCAM Viewer in order to obtain impact and residual velocities, which were calculated dividing the travelled distance of the projectile between two following digital frames and the corresponding time interval.

Fig. 3 shows the UT results based on a phased-array probe (2.25 MHz, 64 elements). More extended delaminated areas can be observed in the INT structures than in the SAN structures from the back side, but the contrast of the former is more slight than the latter. On the contrary, less extended damaged areas are observed from the front side of the impacts. This is because the damaged areas are more extended in the INT structures but the impact energies are more concentrated on the central locations of the impacts due to the multiple basalt-carbon interfaces.

Fig. 4 shows the 100 μm resolution CT slices. The top-view slices were obtained from a mediate thickness ($\sim 2mm$). The side-view slices are obtained at the impact central locations. It can be observed that the delaminations were generated at the near-surface interfaces between the skin layers and the core layers in the SAN structures. On the contrary, the damages are more generated and extended in the central thickness in the INT structures. For the INT structures, the contrast of slices is relatively lower than for the SAN slices, and therefore it is difficult to identify and even measure these damages quantitatively.

Both UT and CT indicate that the impact energies were converted into either more delaminations due to the lower interlaminar shear strength or more splitting damages due to the inherent limited ductility. These phenomena will be studied and compared by ECPT and then validated by FEA in this paper.

3. METHODOLOGY

A. Experiments

ECPT involves multi-physical interactions with electromagnetic-thermal phenomena including induced eddy currents, Joule heating, and heat conduction [25]. Fig. 5a shows the ECPT schematic configuration in the transmission mode used in this paper. The induction heater (7 kW) generates a pulse excitation signal (150 kHz, 0.2 s duration), which is a period of high-frequency alternating current with high amplitude. The current is then driven into an inductive coil (10 cm × 10 cm, see Fig. 5b) positioned on the front side of the impacted surface of the specimens with a small distance. An infrared camera FLIR SC5000 (320 × 256 pixels, 150 fps) was used to record the temperature profile (2 s duration).

When the current passes through the coil, it generates eddy currents. These eddy currents are related to a subsurface penetration depth δ, based on an exponentially dampened skin effect.

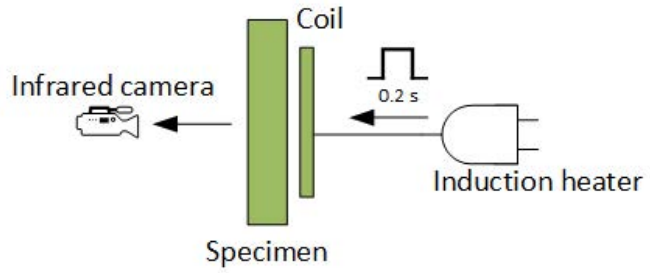

(a)

(b)

Fig. 5. (a) ECPT schematic configuration, (b) coil.

The latter can be calculated from:

$$\delta = (\pi \mu \sigma f)^{-1/2} \quad \textbf{(1)}$$

where f is the excitation frequency, σ is the electrical conductivity, and μ is the magnetic permeability.

The temperature of conductive material increases due to resistive heating from the induced eddy current, which is known as Joule heating. It can be expressed as:

$$Q = \frac{1}{\sigma} \mid J_s \mid^2 = \frac{1}{\sigma} \mid \sigma E \mid^2 \quad \textbf{(2)}$$

where Q is the sum of the generated energy, J_s is the eddy current density [26].

For basalt-carbon fibers hybrid laminates, the thermal diffusion behavior is complex and it is dependent on the structures because carbon fiber is conductive while basalt fiber is insulating.

B. Infrared Image Processing

B.1. PPT

PPT [27] can extract amplitude and phase images using Fourier transform (FT). It provides the possibility to obtain quantitative results in a straightforward manner. Phase is more useful than amplitude because it can retrieve a deeper information. In addition, phase is less affected by environmental reflections, emissivity variations, non-uniform heating, surface geometry and orientation [28].

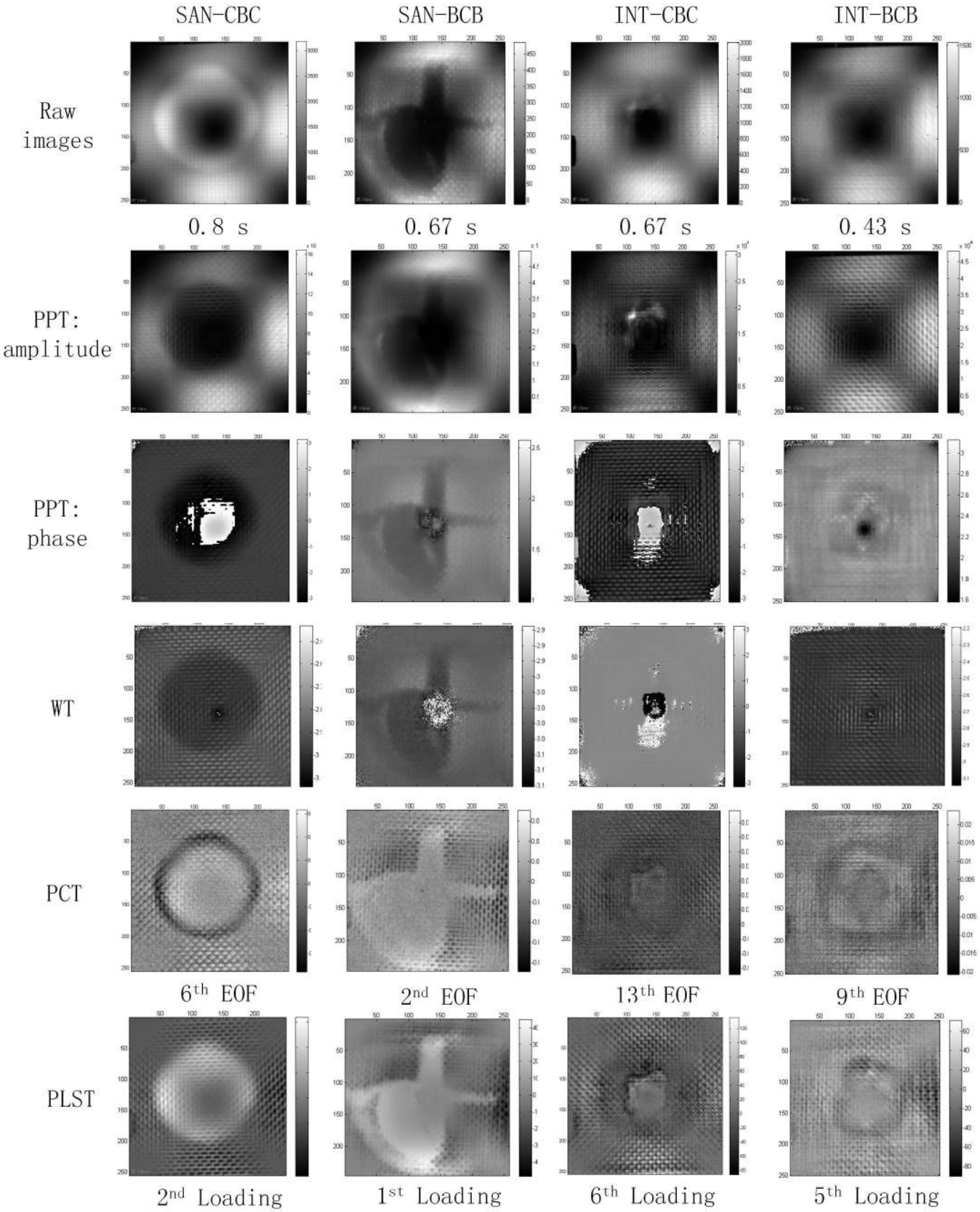

Fig. 6. ECPT results.

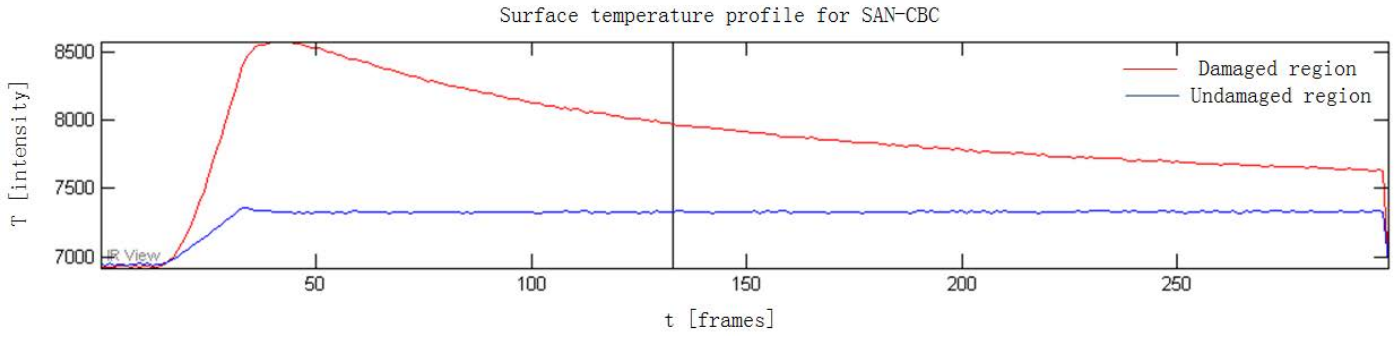

(a) SAN-CBC

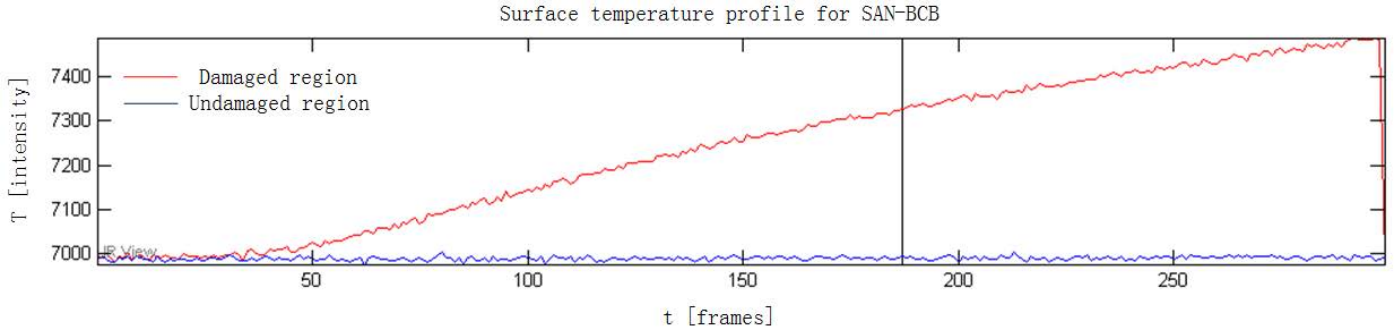

(b) SAN-BCB

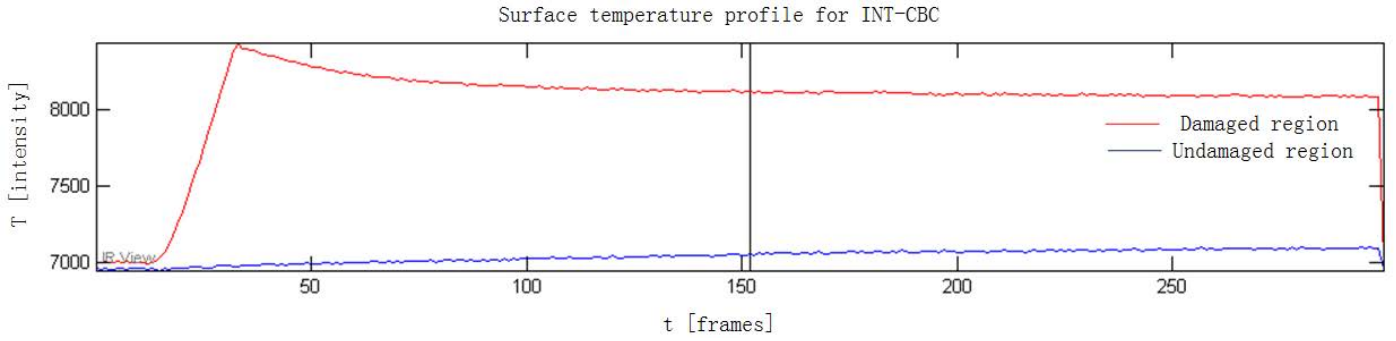

(c) INT-CBC

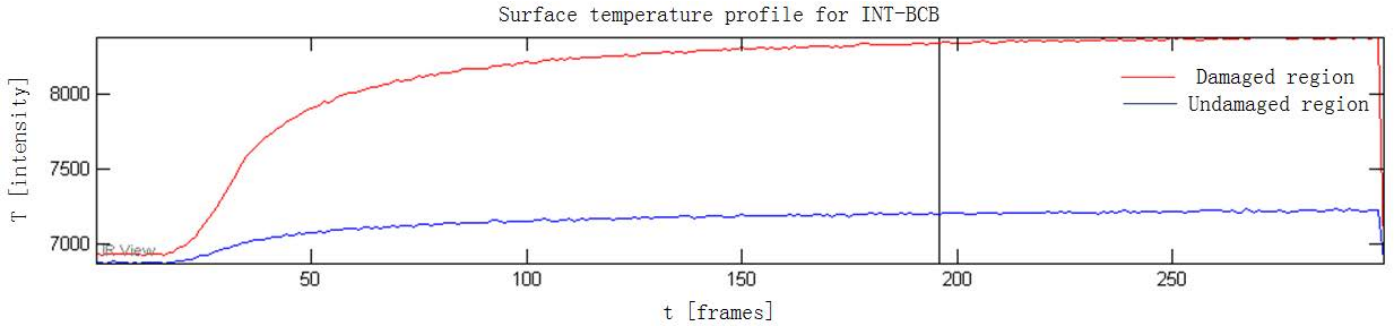

(d) INT-BCB

Fig. 7. Surface temperature profile curves for both damaged (red color) and undamaged (blue color) regions.

B.2. WT

WT can generate a collection of time-frequency representations of the signal and with different resolutions [29]. A complex Morlet wavelet, as recommended in [30], was selected as the mother wavelet. The translation factor T (related to recorded time) with the fixed scale factor S (related to frequency) of 200 were also used.

B.3. PCT

PCT [31] can extract image features and reduce undesirable signals. Different from classical principal component analysis, PCT relies on singular value decomposition (SVD) which extracts spatial and temporal data from a matrix in a compact manner by projecting original data onto empirical orthogonal functions (EOFs). Original features can often be adequately represented by only a few EOFs. PCT is also suitable to be combined with other image processing techniques, *e.g.*, in [32–34].

B.4. PLST

PLST [35] is based on a statistical correlation method known as partial least squares regression (PLSR). It computes Loading and Score vectors which are correlated to the predicted block, while describing a large amount of the variations in the predictor matrix. The matrix corresponds to the obtained surface temperature.

C. SNR Analysis

SNR is used in this paper as a means to compare the sensitivity of the applied image processing algorithms. SNR is expressed in decibels (dB) following the 20 log rule which is often used in imaging applications, as follows [36]:

$$SNR = 20 \cdot log_{10} \mid \frac{S_d - S_a}{\sigma_{Sa}} \mid \quad (3)$$

where S_d is the signal intensity, S_a is the sound area intensity, and σ_{Sa} is the standard deviation which represents the noise variability.

SNR analysis can provide important references for the sensitivity of each technique when it is used to compare the detectability of similar features or defects.

D. Finite Element Analysis

Numerical simulations were performed using COMSOL Multiphysics. 100 mm square geometry of the layer/woven fabrics were built. There are 6.7 warps/cm and 7.7 wefts/cm for basalt fiber layers, while there are 3.9 warps/cm and 4.1 wefts/cm for carbon fiber layers. A homogeneous isotropic steel sphere with the diameter of 7.5 mm and the mass of 1.725 g was built to correspond to the experiments. The same impact speeds to the experiments were set up at 253.46 m/s for SAN and 230.74 m/s for INT (see Section 2).

Taking into account the peculiarities of the structure, the mesh was built by tetrahedral elements. After the construction of the mesh, the materials used for the fabrication were assigned by linking each layer to the proper values of Young's modulus and density, respectively. In Table 2, these values are reported both for the fibers and the steel that constitutes the bullet.

Table 2. Material properties used for modeling

Structure	Young's modulus E $[GPa]$	Density ρ $[kg/m^3]$
Basalt	93	2630
Carbon	230	1780
Steel	205	7820

4. RESULT ANALYSIS

Fig. 6 shows the ECPT results. Compared to CT slices (see Fig. 4), ECPT images have a higher contrast, and therefore the damages can be seen more clearly. Compared to UT (see Fig. 3), ECPT can provide more damage details such as more concentrated impact energies or more extended delaminated areas by various contrast.

In Fig. 6, PPT amplitude shows a similar performance to the raw thermographic images because both of them represent the amplitude characterizations of the thermal signals. WT and PPT phase show a similar image feature. This is understandable because WT can be considered as an extension of FT which preserves time information and it is correlated to the damage depth which maintains the features from FT. In wavelet analysis, a fully scalable modulated window was used instead of a fixed truncation window used in FT. PCT and PLST provide the most features and they show a similar performance because both of them extract the main image characteristics by regressing the thermal signal time matrix.

An interesting phenomenon can be found in the temperature profile curves in Fig. 7. For the CBC structures, a temperature ascent-descent behavior can be observed clearly as shown in Figs. 7a and 7c. However, only a temperature ascent behavior can be observed for the BCB structures as shown in Figs. 7b and 7d. This is because eddy current was only generated in the conductive carbon fiber layers, and it did not exist in the insulating basalt fiber layers. Therefore, the surface temperature profiles only show a heating behavior for the insulating basalt fiber skins in the BCB structures.

In the SAN-CBC temperature profile as shown in Fig. 7a, higher temperature values are reached for both damaged (red color) and undamaged (blue color) regions than the temperature values in the SAN-BCB structure (see Fig. 7c). This is because according to Eqs. 1 and 2, there is a higher generated energy in the thicker 5-layer carbon fiber skin in the SAN-CBC structure than in the INT-CBC structure which only has a 2-layer carbon fiber skin. On the contrary, a lower energy was generated in the SAN-BCB structure (see Fig.7b) than in the INT-BCB structure (see Fig. 7d) because the former has a thicker 7-layer insulating basalt fiber skin than the latter which only has a 2-layer insulating basalt fiber skin.

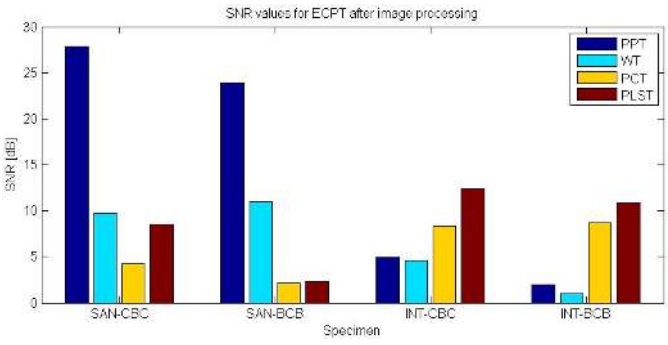

Fig. 8. SNR values for ECPT after different image processing.

Fig. 8 shows the SNR values for ECPT applying PPT phase,

WT, PCT and PLST algorithms. For the SAN structures, PPT and WT have larger SNR values than PCT and PLST. On the contrary, the former has smaller SNR values than the latter in the INT structure. This indicates that PPT and WT which are both based on FT are more suitable to the detection of the delaminations between the skin and the core layers in the SAN structures, while PCT and PLST are more suitable to the evaluation of interlaminar damages in the INT structures. Specifically, PPT shows a higher contrast than WT, while PLST shows a higher contrast than PCT.

As discussed in Section 2 and as validated by CT in Fig. 4, The INT structure has more extended damaged areas, but the impact energies were converted into splitting damages more at the central locations of the impacts. This is the reason why PCT and PLST are more suitable, because they are more sensitive to small feature identifications. On the contrary, PPT and WT are less affected by the sound area noise. The FEA results in Fig. 9 can also validate that the extended damaged areas in the INT structures are larger, which corresponds to the discussions in this paper.

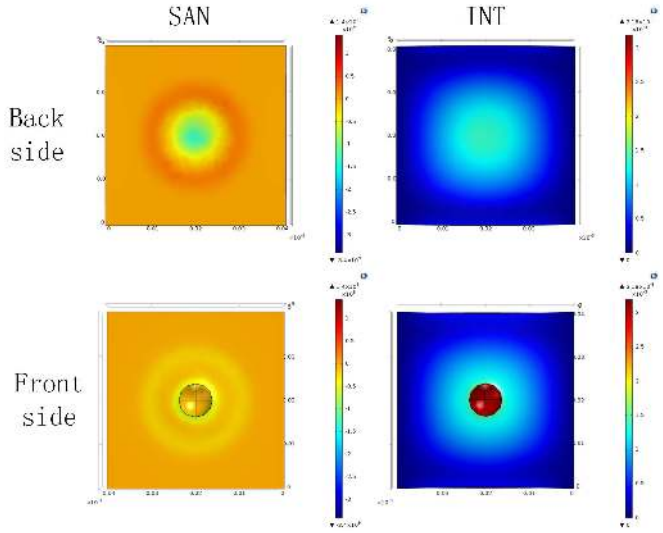

Fig. 9. FEA results.

5. CONCLUSIONS

ECPT can be used to evaluate basalt-carbon hybrid fiber-reinforced polymer composite laminates. It can provide a higher contrast and a better image performance than CT, while it can also provide more detailed information than UT.

Different surface temperature profile behaviors are observed for the CBC and the BCB stacking sequences, respectively. This is due to eddy current that can only be generated in the conductive carbon fiber layers. More detailed analysis has been done in the context.

Image processing can improve the image performance for ECPT. Specifically, PPT and WT are more suitable to the SAN structures, while PLST and PCT are more suitable to the INT structures.

Absorbed energies are more easily converted into delamination in the SAN structures due to the lower interlaminar shear strength. On the contrary, it is more easily converted into splitting damages in the INT structures due to the inherent limited ductility. More extended damaged areas are generated in the INT structures, but the impact energies are more concentrated on the impact locations due to the multiple basalt-carbon interfaces. FEA was performed and it validated the above-mentioned discussions.

FUNDING

Canada Research Chair: Multipolar Infrared Vision (MiViM);
Natural Sciences and Engineering Research Council (NSERC) Canada: Discovery Grant;
Fonds de recherche du Québec - Nature et technologies (FRQNT): International Internship Program no. 211450;
Regroupement pour l'étude des environnements partagés intelligents répartis (REPARTI): International Internship Program no. 211450.

REFERENCES

1. S. Sfarra, F. López, F. Sarasini, J. Tirillò, L. Ferrante, S. Perilli, C. Ibarra Castanedo, D. Paoletti, E. J. Barbero, and X. Maldague, "Analysis of damage in hybrid composites subjected to ballistic impacts: an integrated non-destructive approach," in "Handbook of Composites from Renewable Materials, Physico-Chemical and Mechanical Characterization," V. K. Thakur, M. K. Thakur, and M. R. Kessler, eds. (John Wiley & Sons, 2017), pp. 175–210.
2. F. Sarasini, J. Tirillò, L. Ferrante, M. Valente, T. Valente, L. Lampani, P. Gaudenzi, S. Cioffi, S. Iannace, and L. Sorrentino, "Drop-weight impact behaviour of woven hybrid basalt–carbon/epoxy composites," Compos. Part B: Eng. **59**, 204–220 (2014).
3. R. Petrucci, C. Santulli, D. Puglia, E. Nisini, F. Sarasini, J. Tirillò, L. Torre, G. Minak, and J. Kenny, "Impact and post-impact damage characterisation of hybrid composite laminates based on basalt fibres in combination with flax, hemp and glass fibres manufactured by vacuum infusion," Compos. Part B: Eng. **69**, 507–515 (2015).
4. A. K. Bandaru, L. Vetiyatil, and S. Ahmad, "The effect of hybridization on the ballistic impact behavior of hybrid composite armors," Compos. Part B: Eng. **76**, 300–319 (2015).
5. G. Czél and M. Wisnom, "Demonstration of pseudo-ductility in high performance glass/epoxy composites by hybridisation with thin-ply carbon prepreg," Compos. Part A: Appl. Sci. Manuf. **52**, 23–30 (2013).
6. M. Jalalvand, G. Czél, and M. R. Wisnom, "Damage analysis of pseudo-ductile thin-ply ud hybrid composites–a new analytical method," Compos. Part A: Appl. Sci. Manuf. **69**, 83–93 (2015).
7. H. Yu, M. L. Longana, M. Jalalvand, M. R. Wisnom, and K. D. Potter, "Pseudo-ductility in intermingled carbon/glass hybrid composites with highly aligned discontinuous fibres," Compos. Part A: Appl. Sci. Manuf. **73**, 35–44 (2015).
8. N. Naik, R. Ramasimha, H. Arya, S. Prabhu, and N. ShamaRao, "Impact response and damage tolerance characteristics of glass–carbon/epoxy hybrid composite plates," Compos. Part B: Eng. **32**, 565–574 (2001).
9. M. Hosur, M. Adbullah, and S. Jeelani, "Studies on the low-velocity impact response of woven hybrid composites," Compos. Struct. **67**, 253–262 (2005).
10. E. Sevkat, B. Liaw, F. Delale, and B. B. Raju, "Drop-weight impact of plain-woven hybrid glass–graphite/toughened epoxy composites," Compos. Part A: Appl. Sci. Manuf. **40**, 1090–1110 (2009).
11. M. M. Thwe and K. Liao, "Durability of bamboo-glass fiber reinforced polymer matrix hybrid composites," Compos. science technology **63**, 375–387 (2003).
12. T. Deák and T. Czigány, "Chemical composition and mechanical properties of basalt and glass fibers: a comparison," Textile Res. J. **79**, 645–651 (2009).
13. X. Maldague, *Theory and practice of infrared technology for nondestructive testing* (Wiley, 2001).
14. H. Fernandes, H. Zhang, A. Figueiredo, C. Ibarra-Castanedo, G. Guimarares, and X. Maldague, "Carbon fiber composites inspection and defect characterization using active infrared thermography: nu-

merical simulations and experimental results," Appl. Opt. **55**, D46–D53 (2016).
15. S. Boccardi, G. M. Carlomagno, and C. Meola, "Basic temperature correction of qwip cameras in thermoelastic/plastic tests of composite materials," Appl. Opt. **55**, D87–D94 (2016).
16. V. Vavilov, Y. Y. Pan, and D. Nesteruk, "Infrared thermographic inspection of water ingress in composite honeycomb panels." Appl. Opt. **55**, D120–D125 (2016).
17. H. Zhang, F. Robitaille, C. U. Grosse, C. Ibarra-Castanedo, J. O. Martins, S. Sfarra, and X. P. Maldague, "Optical excitation thermography for twill/plain weaves and stitched fabric dry carbon fibre preform inspection," Compos. Part A: Appl. Sci. Manuf. **107**, 282–293 (2018).
18. H. Zhang, S. Sfarra, F. Sarasini, C. Ibarra-Castanedo, S. Perilli, H. Fernandes, Y. Duan, J. Peeters, N. P. Avelidis, and X. Maldague, "Optical and mechanical excitation thermography for impact response in basalt-carbon hybrid fiber-reinforced composite laminates," IEEE Transactions on Ind. Informatics **14**, 514–522 (2018).
19. H. Zhang, H. Fernandes, F. B. D. Dizeu, U. Hassler, J. Fleuret, M. Genest, C. Ibarra-Castanedo, F. Robitaille, S. Joncas, and X. Maldague, "Pulsed micro-laser line thermography on submillimeter porosity in carbon fiber reinforced polymer composites: experimental and numerical analyses for the capability of detection," Appl. Opt. **55**, D1–D10 (2016).
20. K. Ahi, S. Shahbazmohamadi, and N. Asadizanjani, "Quality control and authentication of packaged integrated circuits using enhanced-spatial-resolution terahertz time-domain spectroscopy and imaging," Opt. Lasers Eng. **104**, 274–284 (2018).
21. K. Ahi, "Review of gan-based devices for terahertz operation," Opt. Eng. **56**, 090901 (2017).
22. K. Ahi, "Mathematical modeling of thz point spread function and simulation of thz imaging systems," IEEE Transactions on Terahertz Sci. Technol. **7**, 747–754 (2017).
23. H. Zhang, S. Sfarra, K. Saluja, J. Peeters, J. Fleuret, Y. Duan, H. Fernandes, N. Avdelidis, C. Ibarra-Castanedo, and X. Maldague, "Non-destructive investigation of paintings on canvas by continuous wave terahertz imaging and flash thermography," J. Nondestruct. Eval. **36**, 34 (2017).
24. H. Zhang, L. Yu, U. Hassler, H. Fernandes, M. Genest, F. Robitaille, S. Joncas, W. Holub, Y. Sheng, and X. Maldague, "An experimental and analytical study of micro-laser line thermography on micro-sized flaws in stitched carbon fiber reinforced polymer composites," Compos. Sci. Technol. **126**, 17–26 (2016).
25. A. Yin, B. Gao, G. Yun Tian, W. Woo, and K. Li, "Physical interpretation and separation of eddy current pulsed thermography," J. Appl. Phys. **113**, 064101 (2013).
26. G. Y. Tian, Y. Gao, K. Li, Y. Wang, B. Gao, and Y. He, "Eddy current pulsed thermography with different excitation configurations for metallic material and defect characterization," Sensors. **16**, 843 (2016).
27. X. Maldague and S. Marinetti, "Pulse phase infrared thermography," J. applied physics **79**, 2694–2698 (1996).
28. C. Ibarra-Castanedo and X. P. Maldague, "Infrared thermography," in "Handbook of technical diagnostics," H. Czichos, ed. (Springer Berlin Heidelberg, 2013), pp. 175–220.
29. G. Kaiser, *A friendly guide to wavelets* (Springer Science & Business Media, 2010).
30. X. Maldague, F. Galmiche, and A. Ziadi, "Advances in pulsed phase thermography," Infrared physics & technology **43**, 175–181 (2002).
31. N. Rajic, "Principal component thermography for flaw contrast enhancement and flaw depth characterisation in composite structures," Compos. Struct. **58**, 521–528 (2002).
32. B. Yousefi, S. Sfarra, C. I. Castanedo, and X. P. Maldague, "Comparative analysis on thermal non-destructive testing imagery applying candid covariance-free incremental principal component thermography (ccipct)," Infrared Phys. & Technol. **85**, 163–169 (2017).
33. B. Yousefi, S. Sfarra, C. I. Castanedo, and X. P. Maldague, "Thermal ndt applying candid covariance-free incremental principal component thermography (ccipct)," in "Thermosense: Thermal Infrared Applications XXXIX," , vol. 10214 (International Society for Optics and Photonics, 2017), vol. 10214, p. 102141I.
34. B. Yousefi, H. M. Sharifipour, C. I. Castanedo, and X. P. Maldague, "Automatic irndt inspection applying sparse pca-based clustering," in "Electrical and Computer Engineering (CCECE), 2017 IEEE 30th Canadian Conference on," (IEEE, 2017), pp. 1–4.
35. F. Lopez, C. Ibarra-Castanedo, V. de Paulo Nicolau, and X. Maldague, "Optimization of pulsed thermography inspection by partial least-squares regression," NDT & E Int. **66**, 128–138 (2014).
36. M. A. Choma, M. V. Sarunic, C. Yang, and J. A. Izatt, "Sensitivity advantage of swept source and fourier domain optical coherence tomography," Opt. express **11**, 2183–2189 (2003).